T. Ludwig, M. Doreille, S. Merazzi, R. Vescovini, C. Bisagni
Dynamic Finite Element Simulations of Composite Stiffened Panels with a Transverse-Isotropic Viscoelastic Energy Dissipation Model
Progress in Aerospace Sciences, Vol. 78, 2015, p. 30-38
doi:10.1016/j.paerosci.2015.06.001

Dynamic finite element simulations of composite stiffened panels with a transverse-isotropic viscoelastic energy dissipation model

Thomas Ludwig[a,1], Mathias Doreille[a], Silvio Merazzi[a], Riccardo Vescovini[b], Chiara Bisagni[b]

[a] *SMR Engineering & Development, CH-2502 Bienne, Switzerland*
[b] *Dipartimento di Scienze e Tecnologie Aerospaziali, Politecnico di Milano, Via La Masa 34, 20156 Milano, Italy*

Abstract

This paper presents a methodology for predicting the damped response and energy dissipation of laminated composite structures, subjected to dynamic loads. Starting from simple coupon tests to characterize the material, the numerical simulation of damping properties is made possible by a novel linear viscoelastic model that has been developed and implemented in the finite element code B2000++. A nonlinear optimization procedure is adopted to fit experimental data and define the exponential Maxwell parameter model. To illustrate the potentialities of the method, the post-buckling analysis of a relatively complex aeronautical panel is presented, accounting not only for geometric nonlinearities, but also for viscoelastic effects. The results illustrate the effects due to material dissipation, their relation to the effects of inertia, and the influence of geometric imperfections on the response of the panel.

Keywords: Viscoelastic, Damping in Composite Materials, Dynamic Loads, Post-Buckling, Numerical Damping Effects

Contents

Email address: tludwig@smr.ch (Thomas Ludwig)
[1] Principal corresponding author

1. Introduction

Post-buckling analysis of aeronautical panels is often conducted assuming static or quasi-static conditions. But the nature of real structures is intrinsically dynamic, and in many operating conditions the structure experiences loading conditions that cannot be considered static. This is the case, for instance, of a gust or a sudden landing. Under these circumstances, the structural response can be affected not only by geometric nonlinearities, but also by the material's dissipative behavior.

Dissipation effects in composite materials have been the subject of many studies, a comprehensive review can be found in Chandra et al. (1999). However, most of the methods that are described in these studies are restricted to linear assumptions, such as the method of McTavish and Hughes (1993), the anelastic displacement fields damping model (Enelund and Lesieutre, 1999), and frequency-domain solution procedures with the assumption of steady-state forced oscillatory conditions (Vasques et al., 2010; Bobillot and Balmes, 2002). Modal damping can be used in the context of a direct time integration procedure after introducing globally defined constant damping matrices, reflecting viscous damping at one single frequency.

While the assumption of linear behavior is advantageous from the computational point-of-view, it precludes from predicting important phenomena such as buckling, frequency-dependence, and local effects in the case where the structure consists of different materials. Therefore, the assumption of linear behavior is not valid when assessing the damping effects on the panel's response in the post-buckling field.

In the context of nonlinear methods, the approach that is usually adopted is the direct time integration of the generalized Maxwell convolution integral. The numerical processing of

viscoelastic equations has been discussed by Schapery (1961), and Gradowczyk and Moavenzadeh (1969). An early procedure based on the convolution integral, although limited to stationary analysis (creep) and using the finite-difference method, has been presented by one of the authors (Merazzi and Stehlin, 1977).

Few works in the past have considered the numerical simulation of relatively complex aircraft structures that are designed to operate in the post-buckling field, accounting for nonlinear damping effects, despite the potential influence of these effects on the structure's response. The advances in computational power and finite element technology allow nowadays to tackle industrial-size problems, including the study of structural subcomponents or even aircraft models.

In the present work, a novel analysis procedure is proposed to account for nonlinear damping during the numerical simulation of carbon-fiber reinforced plastic (CFRP) aeronautical panels. It relies on the experimental characterization of the material dissipation properties by means of Dynamic Mechanical Analysis (DMA), and on the numerical simulation of the material viscoelastic behavior referring to the Generalized Maxwell Model (GMM). The resulting nonlinear problem is solved by an implicit transient analysis method with the B2000++ finite element analysis package (SMR S.A., 1999-2014). It makes use of a multistep backward differential formula method for time integration (Shampine and Gear, 1979), with a variable time increment (Nordsieck, 1962).

The body of this paper is organized as follows: first, a description of the numerical procedures to implement the GMM in the finite element code is provided. Then, the experimental characterization of a CFRP material is explained together with the strategies for the parameter fitting of the experimental results. An application of the GMM for computing dynamic response of a composite stiffened curved panel loaded in compression and working in the post-buckling field is presented.

2. The Generalized Maxwell Model (GMM)

2.1. One dimensional linear GMM

For the sake of completeness, a brief description of the Generalized Maxwell Material (GMM) is presented, following the approach of Simo and Hughes (2000) where infinitesimal strains are assumed. A GMM consists of N Maxwell elements that are assembled in parallel. Each Maxwell element is represented by a spring with elastic modulus E_i and a dashpot (damping element) with relaxation time τ_i, as reported in Figure 1. E_∞ is the elastic modulus at full relaxation, and the instantaneous elastic modulus E_0 is

$$E_0 = E_\infty + \sum_{i=1}^{N} E_i \tag{1}$$

Introducing the non-dimensional relative moduli of the Maxwell elements

$$\gamma_i = \frac{E_i}{E_0} \tag{2}$$

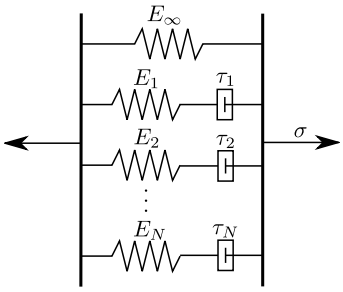

Figure 1: Schematic representation of a Generalized Maxwell Model.

and

$$\gamma_\infty = \frac{E_\infty}{E_0} \tag{3}$$

The expression for γ_∞ is obtained:

$$\gamma_\infty = 1 - \sum_{i=1}^{N} \gamma_i \tag{4}$$

Using these definitions, the normalized generalized Maxwell relaxation function can be written as

$$g(t) = \gamma_\infty + \sum_{i=1}^{N} \gamma_i e^{-t/\tau_i} \tag{5}$$

where τ_i is the relaxation time of the i-th Maxwell element. The constitutive equation of a GMM, in this case for a one-dimensional linear material and infinitesimal strains, consists of the convolution integral

$$\sigma(t) = \int_{u=-\infty}^{t} g\,(t-u)\,\dot{s}_0(u)\mathrm{d}u \tag{6}$$

with $\sigma(t)$ the stress and

$$\dot{s}_0 = E_0\dot{\epsilon} = \frac{E_\infty}{\gamma_\infty}\dot{\epsilon} \tag{7}$$

representing the time-derivative of the instantaneous stress($\dot{\epsilon}$ is the time-derivative of the strain).

2.2. Extension to transverse-isotropic materials

In two and three dimensions, the normalized generalized Maxwell relaxation function g becomes a fourth-order tensor.

Time-independence is assumed for the Poisson ratios, while different relaxation functions are introduced for the fiber, matrix and shear directions. By exploiting the symmetry conditions for transverse isotropy and adopting Voigt notation as proposed by Melo and Radford (2003), g can be written as:

$$g = \begin{bmatrix} g_1 & 0 & 0 & 0 & 0 & 0 \\ 0 & g_2 & 0 & 0 & 0 & 0 \\ 0 & 0 & g_2 & 0 & 0 & 0 \\ 0 & 0 & 0 & g_2 & 0 & 0 \\ 0 & 0 & 0 & 0 & g_6 & 0 \\ 0 & 0 & 0 & 0 & 0 & g_6 \end{bmatrix}$$

$$\forall j \in \{1,2,6\}: \quad g_j(t) = \gamma_{\infty,j} + \sum_{i=1}^{N} \gamma_{i,j} e^{-t/\tau_{i,j}} \tag{8}$$

Likewise, stress and strain quantities are vectors in Voigt notation, and the time-derivative of the instantaneous stress is

$$\dot{s}_0 = C_0\dot{\epsilon} = (\gamma_\infty)^{-1} C_\infty \dot{\epsilon} \tag{9}$$

with C_0 the instantaneous constitutive matrix, C_∞ the constitutive matrix at relaxation, and

$$\gamma_\infty = \begin{bmatrix} \gamma_{\infty,1} & 0 & 0 & 0 & 0 & 0 \\ 0 & \gamma_{\infty,2} & 0 & 0 & 0 & 0 \\ 0 & 0 & \gamma_{\infty,2} & 0 & 0 & 0 \\ 0 & 0 & 0 & \gamma_{\infty,2} & 0 & 0 \\ 0 & 0 & 0 & 0 & \gamma_{\infty,6} & 0 \\ 0 & 0 & 0 & 0 & 0 & \gamma_{\infty,6} \end{bmatrix} \tag{10}$$

2.3. Other extensions of the GMM

The damping model can be extended with an additive split of the strain into deviatoric and volumetric strain parts, using separate constitutive equations for each part of the strain. This approach can be appropriate for nearly incompressible materials where the bulk response is elastic and only the deviatoric response is viscoelastic.

In the case of hyperelastic and finite strain materials the expression $C_0\epsilon$ must be replaced by $\partial W_0/\partial\epsilon$, where W_0 is the instantaneous stored energy function.

2.4. The recurrence relationship

The GMM cannot be directly employed within a time-integration ordinary differential equation (ODE) solver, as the convolution integral $g(t_n)$ would have to be recomputed at each time step t_n. Thus, the implementation would have quadratic complexity w.r.t. the number of time steps.

Using the algebraic property of the exponential function and some time integration approximations, the convolution integral can be transformed to the recurrence relationship:

$$\begin{aligned} t_{n+1} &= t_n + \Delta t_n \\ s_{0,n+1} &= C_0\epsilon_{n+1} \\ h^{(i)}_{n+1} &= e^{-\Delta t_n/\tau_i} h^{(i)}_n + e^{-\Delta t_n/2\tau_i}\left(s_{0,n+1} - s_{0,n}\right) \\ \sigma_{n+1} &= \gamma_\infty s_{0,n+1} + \sum_{i=1}^{N} \gamma_i h^{(i)}_{n+1} \end{aligned} \tag{11}$$

where

$$h^{(i)}_n \approx \int_{u=-\infty}^{t_n} e^{-(t_n-u)/\tau_i}\,\dot{s}\,\mathrm{d}u \tag{12}$$

represents the internal stress state of the i-th Maxwell element at time step t_n.

Implementing this recurrence relationship within a time-integration ODE solver requires only the computation of a single recurrence iteration for each time step (and for each Newton iteration at this time step in case of nonlinear analysis). However, the N internal stress state variables $h^{(i)}_n$ have to be stored at each integration point of each finite element.

2.5. Free and dissipated energy

Staverman and Schwarzl (1952) give an expression for the Helmholtz free energy F for a GMM in one dimension. In Del Piero and Deseri (1996) this expression is generalized to three-dimensional linear viscoelasticity:

$$F = \frac{1}{2}\int_{u=-\infty}^{t}\int_{v=-\infty}^{t} g(2t-u-v)\dot{\epsilon}(u)\,C_0\dot{\epsilon}(v)\,\mathrm{d}u\mathrm{d}v \tag{13}$$

Using the definition of the Helmholtz free-energy $F = U - T_0\theta$, where $U = \sigma\epsilon$ is the internal energy, T_0 is the constant temperature, and θ is the entropy, time-differentiation leads to

$$\sigma\dot{\epsilon} = \dot{F} + T_0\dot{\theta} \tag{14}$$

where $\dot{\theta}$ is the rate of entropy production. By time-differentiation of F, the rate of dissipated energy $D = T_0\dot{\theta}$ is obtained as

$$D = -\int_{u=-\infty}^{t}\int_{v=-\infty}^{t} \frac{\mathrm{d}g(2t-u-v)}{\mathrm{d}t}\dot{\epsilon}(u)\,C_0\dot{\epsilon}(v)\,\mathrm{d}u\mathrm{d}v \tag{15}$$

A practicable evaluation of the above expression is achieved by using the recurrence definition of $h^{(i)}_n$ and the semi-group property of g. The free strain energy per unit volume F_n and the rate of dissipated strain energy per unit volume D_n at the time step t_n can be expressed as:

$$F_n = \frac{\gamma_\infty}{2} s_{0,n}\epsilon_n + \frac{1}{2}\sum_{i=1}^{N}\gamma_i h^{(i)}_n S_0 h^{(i)}_n \tag{16}$$

$$D_n = \sum_{i=1}^{N}\frac{\gamma_i}{\tau_i} h^{(i)}_n S_0 h^{(i)}_n \tag{17}$$

where $S_0 = (C_0)^{-1}$ is the instantaneous compliance matrix.

3. Experimental characterization of CFRP and GMM parameter fitting

3.1. Dynamic Mechanical Analysis (DMA)

The CFRP material studied experimentally was Hexcel® IM7/8552, its mechanical characteristics being known (Bisagni et al., 2011). To measure the loss factors, a number of Dynamic Mechanical Analysis (DMA) tests were carried out (Bisagni and Catapano, 2013).

The tests were performed in a dual cantilever bending configuration at the Politecnico di Milano using a TA Instruments DMA 2980. The equipment is controlled by means of software called TA Advantage Control. In the dual cantilever configuration, the specimen was clamped on its ends, and a central probe, controlled by a pneumatic system and constrained to the specimen, bent it, as shown in Figure 2.

The tests allowed to analyze the behavior of the material at different frequencies. In particular, the storage modulus, the loss modulus and the loss factor of the specimen were measured. In order to obtain the in-plane shear loss factor using

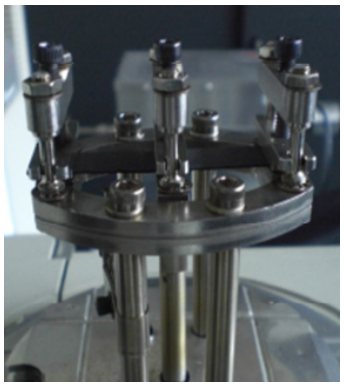

Figure 2: Experimental setup.

only flexural tests, the viscoelastic model presented by Melo and Radford (2003) is employed.

The specimen geometry is imposed by the test type and depends on the material properties. Due to the equipment limitations for what concerns the minimum and maximum applicable force and displacement, the specimens were manufactured with a length of 60 mm, a width of 10 mm and 6 unidirectional plies. Specimens with fibers oriented at 0°, 30°, 45° and 90° were tested. The thickness of each single ply is 0.125 mm, and the total thickness of the specimen is 0.75 mm

A sinusoidal controlled mode with amplitude of $15 \cdot 10^{-6}$ m was used, at a temperature of 35 °C. Three or four specimens were tested for each fiber orientation from 0 to 50 Hz. Only the 90° specimens were not tested at 50 Hz, because the central probe was not able to sustain the vibration for at least the seven cycles required by the equipment in order to identify the complex modulus and the loss factor.

The mean loss factor of the 0° specimens varied between 0.007 and 0.004 for frequencies ranging from 0.5 to 10 Hz, exactly the same result obtained by Melo and Radford (2004) using identical fibers.

3.2. GMM parameter fitting

The DMA measurements were attributed to the components as reported in Table 1.

0°	$\longrightarrow$	1 (fiber)
90°	$\longrightarrow$	2 (matrix)
0°,30°,45°,90°	$\longrightarrow$	6 (shear)

Table 1: Attribution of DMA measurements to the components.

The fitting of the GMM parameters in the frequency domain, against the measured relative storage moduli $\bar{\gamma}'_j$ and loss moduli $\bar{\gamma}''_j$, was carried out as follows. The numerical relative storage moduli γ'_j and loss moduli γ''_j can be calculated from the GMM parameters $\gamma_{i,j}$ and $\tau_{i,j}$:

$$\forall j \in \{1,2,6\} : \begin{cases} \gamma'_j(f) &= \sum_{i=1}^{N} \dfrac{\gamma_{i,j}(\tau_{i,j}2\pi f)^2}{1+(\tau_{i,j}2\pi f)^2} \\ \gamma_j"(f) &= \sum_{i=1}^{N} \dfrac{\gamma_{i,j}\tau_{i,j}2\pi f}{1+(\tau_{i,j}2\pi f)^2} \end{cases} \tag{18}$$

The GMM parameters are obtained by solving the three nonlinear minimization problems

$$\min \int_{f2}^{f1} (\gamma'_j(f) - \bar{\gamma}_j'(f))^2 + (\gamma_j"(f) - \bar{\gamma}_j"(f))^2 df \tag{19}$$

Whether the nonlinear optimization yields a good fit depends on how well the elastic moduli at relaxation correspond with the storage and loss moduli, the number of Maxwell elements N, and the optimization strategy. When N is small, global optimization followed by local optimization can be effective, however, global optimization may fail to converge for larger N. A work-around to this problem is to use only local optimization, but then, the fitted results are often not satisfactory. By fixing the relaxation times $\tau_{i,j}$ to predefined values, the number of fitting parameters is divided by two but, more importantly, the minimization problem becomes easier to solve, and local optimization algorithms can produce a good fit.

Since the frequency ranges of the DMA measurements were rather narrow, a small number of Maxwell elements, $N = 3$, was selected using predefined relaxation times (the same for all components j) in conjunction with a local optimization, using the *BOBYQA* algorithm of the *NLOPT* package (Johnson, 2010). Table 2 contains the fitted parameters and Figure 3 illustrates the results for the fiber direction, for which the absolute loss moduli are greatest.

$\tau_{i,1}[s]$	0.003	0.03	0.3
$\gamma_{i,1}$	$8.697 \cdot 10^{-3}$	$4.798 \cdot 10^{-3}$	$1.287 \cdot 10^{-2}$
$\gamma_{i,2}$	0	$1.405 \cdot 10^{-2}$	$2.048 \cdot 10^{-2}$
$\gamma_{i,6}$	$1.885 \cdot 10^{-2}$	$1.548 \cdot 10^{-2}$	$2.662 \cdot 10^{-2}$

Table 2: Fitted GMM viscoelastic parameters for Hexcel® IM7/8552.

4. Application to a three-stringer stiffened CFRP panel

The GMM was applied to the dynamic (or transient) post-buckling simulation of a stiffened curved composite panel with three blade stringers. Compared to quasi-static analysis, the most prominent phenomenon that is observed in dynamic analysis is that the sudden drops of load at unstable bifurcation points induce local vibrations and stress fluctuations, which are eventually damped out by the GMM.

This panel has a radius of 938 mm, an arc length of 135.9 mm between each pair of stringers, and a free length of 600 mm. The stringer height, measured from the skin mid-surface, is 20 mm. The stringer is connected to the skin by means of two tapered flanges of width equal to 31 mm (this is simplified in the finite element model). The CFRP material is Hexcel® IM7/8552, for which the static material data from (Bisagni et al., 2011) was used (Table 3).

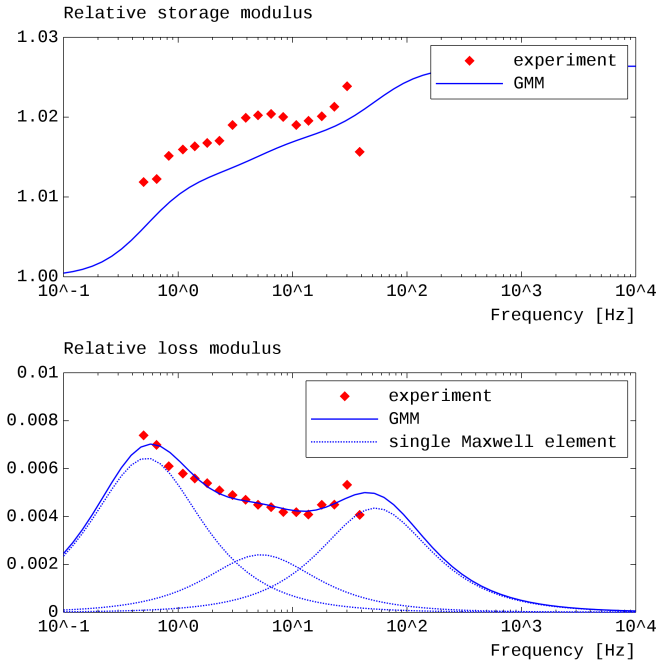

Figure 3: Hexcel® IM7/8552 relative storage and loss moduli in fiber direction ($j = 1$) and approximated GMM with three elements. Dots: Measured. Solid lines: GMM. Dotted lines: Individual Maxwell elements. The relative difference between the measured and the approximated moduli is 6-7% for both curves. The error cannot be brought to zero by employing more Maxwell elements, because both curves are connected and the GMM cannot represent arbitrary curves.

$\bar{E}_{\infty,1}$	150 GPa
$\bar{E}_{\infty,2}$	9.08 GPa
ν	0.32
$\bar{E}_{\infty,6}$	5.29 GPa
ρ	1550 kg/m^3

Table 3: Hexcel® IM7/8552 static material constants and density.

4.1. *Finite element discretization*

The finite element model of the panel is displayed in Figure 4. Unlike the real structure, the model is simplified by assuming stepped flanges of constant thickness.

The FE mesh consists of triquadratic solid elements with 27 nodes. In contrast to the computationally less demanding shell elements, solid elements allow for a more realistic modeling of the junction between the stringer flanges and the stringer web, which can be important when studying mesh convergence. Since the skin and stringer flanges are modeled with separate elements, the material dissipation between skin and stringer flanges can be studied. Concerning the post-buckling behavior and the overall dissipation, and considering the element sizes, a shell element mesh should yield very similar results.

The skin and stringer flanges are each discretized with a single element in the thickness direction, comprising eight plies of the laminate stacking sequence $[0/\pm45/90]_s$ and 12 plies with the stacking sequence $[0_2/\pm45]_3$, respectively. The skin-stringer junction and the stringer web are discretized with two elements, with the same stacking sequence as the stringer flanges.

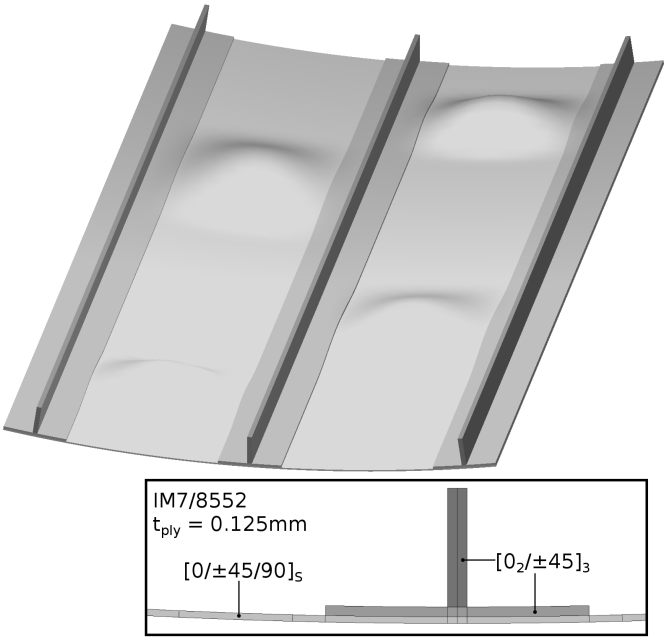

Figure 4: Solid finite element model of three-stringer panel and laminate stacking sequences for the skin and the stringer flange and stringer flange. Imperfections are shown amplified.

Each ply is unidirectional with a thickness of 0.125 mm. An angle of 0° means that the fiber direction is aligned with the axial direction. The material model is the GMM as described in section 2.2, with the static material data of Table 3 and the GMM parameters obtained as described in section 4.5. Numerical quadrature of the first variation, the second variation, etc. is performed separately over each ply. Geometric nonlinearities are accounted for by employing a Total-Lagrangian formulation, using the Green-Lagrange strain and the 2nd Piola-Kirchhoff stress.

An element length of 16 mm, resulting in a mesh with 1672 elements and 18711 nodes, was chosen on the basis of a mesh convergence study, since the buckling load and the post-buckling path do not significantly change with finer meshes. The results obtained with elements of 4, 8 and 16 mm were compared, revealing similar results in terms of buckling load and post-buckling path.

4.2. *Geometric imperfections*

Considering the perfect panel, the first buckling point is unstable, although the drop of load is small, and the panel can be loaded further. But real structures are always characterized by the presence of manufacturing signatures, such as an initial deviation from the nominal geometry. The presence of such imperfections tends to reduce the drop of load at the first buckling, but still allows for secondary instabilities in the post-buckling regime.

The analyses here presented aim to provide a comparison between two opposite scenarios in terms of imperfections. On one hand the perfect panel tends to promote sudden drops of load, whereas the imperfect panel tends to inhibit them.

A geometric deviation of the skin mid-surface was introduced. It approximates the quasi-static post-buckling solution before the transition to global buckling, see Figure 4, and is defined by the formula

$$\begin{aligned} z(x,y) &= A \sum_{i=1}^{4} \cos^2 \bar{x}_i \cos^2 \bar{y}_i \\ \bar{x}_i &= \pi \max\left(-\frac{1}{2}, \min\left(\frac{1}{2}, \frac{x - X_i}{W_i}\right)\right) \\ \bar{y}_i &= \pi \max\left(-\frac{1}{2}, \min\left(\frac{1}{2}, \frac{y - Y_i}{H_i}\right)\right) \end{aligned} \tag{20}$$

with the parameters as shown in Table 4. The amplitude A was chosen by conducting a series of quasi-static post-buckling analyses with different values for A. A value of 0.5 mm was found to be sufficient to bring the drop of load at first buckling to zero. Hence, transient analyses with $A = 0.5$ mm and $A = 0$ (no imperfections) were conducted.

i	X_i	W_i	Y_i	H_i
1	400	150	67.95	135.9
2	200	150	-67.95	135.9
3	90	100	67.95	135.9
4	510	100	-67.95	135.9

Table 4: Numerical parameters for geometric imperfections. The origin of the reference frame is located at the middle stringer on the left border of the panel, the x-axis coincides with the axial direction, the y-axis coincides with the lateral direction, and the z-axis coincides with the opposite radial direction. All values are given in [mm].

It is worth noting this reduction of the drop of load at first buckling could also be achieved by choosing different values for the parameters or altogether by different means, for example by applying a single perturbation force.

Although the kind of imperfection may affect the predicted solution path, its effect on the amplitude of the vibrations following the first buckling should be similar, provided that the drop of load at unstable bifurcation points is reduced by the same amount.

4.3. Quasi-static analysis with linear loading

A linearly increasing edge shortening up to -1.8 mm was applied. This is quite far within the post-buckling field, but below the onset of global buckling. The strains are below 1%, thus, the infinitesimal-strain assumptions required by the GMM are valid.

With a load-controlled quasi-static incremental analysis, a post-buckling solution in the presence of instabilities can be obtained, even for finite element models without geometrical imperfections, by employing artificial damping or stabilization. Adding viscous forces

$$F_{\text{viscous}} = \alpha \frac{1}{\Delta t} M \Delta u \tag{21}$$

where α is a scaling factor, M is the mass matrix, Δu is the vector of incremental displacements, and Δt is the size of the current increment – to the equilibrium equations results in a modified tangent stiffness matrix which remains, in most but not all cases, positive-definite. Which path is followed in the vicinity of bifurcation points is not deterministic and unknown in general; this may depend on a variety of numerical artifacts as well as on the numerical solution parameters. If the solution happens to lie too close to a bifurcation point, convergence may be slow or not be reached altogether. But experience shows that, for the present type of finite element models, this does not occur before global collapse.

The solution algorithm that was applied to the quasi-static analyses is identical to that of the transient analyses (see section 4.6), except for the artificial viscous forces and for the omission of the inertia forces. Its enhanced predictor allowed to utilize a modified Newton method. Compared to a full Newton-Raphson algorithm with a simpler predictor and without an error estimator to control the increment size, but also with artificial damping, the computational effort is reduced by a factor of 3.

The scaling factor α for the artificial damping was calculated such that, for the first increment, the dissipated energy equals 1/10000 of the elastic energy. Otherwise, the same solution parameters, such as the tolerance values for the criterion to test the convergence of the Newton iterations, were used as in the dynamic analyses.

The effect of geometric imperfections can be seen in Figure 5, which compares the load-displacement relationships. At the maximum load, the panel stiffness is reduced to 67% due to the buckling. The deformed pattern at buckling, with and without imperfections, is very similar. However, a different response is observed when the load is increased beyond the buckling load. Mode changes, with buckles moving along the longitudinal direction, characterize the behavior of the nominally perfect panel, while this is not the case for the configuration with geometric imperfections.

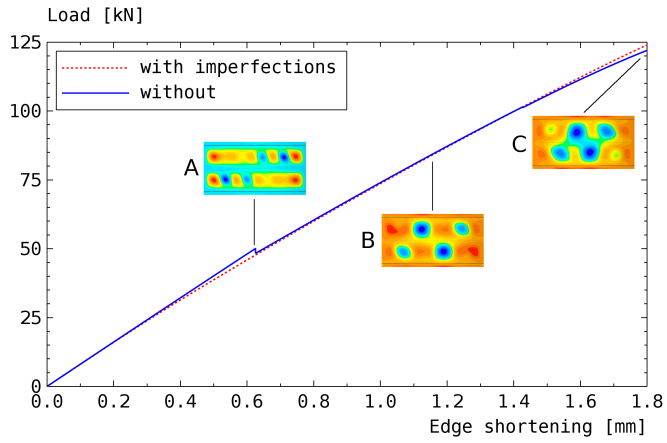

Figure 5: Quasi-static nonlinear analysis with and without imperfections. First buckling occurs around 50 kN. The out-of-plane displacements of the perfect panel are shown as contours for three selected increments. A: at first buckling, before the drop of load. B: in the post-buckling regime. C: at maximum load, before global buckling.

The stress levels are very similar too. The compressive

stress in fiber direction is everywhere below the compressive ply strength of 1200 MPa (in this work only the stress in fiber direction is considered, see (Bisagni et al., 2011) and Camanho et al. (2007) for a detailed characterization of IM7/8552).

4.4. *Dynamic loading conditions*

Assuming that the panel is integrated in the lower fuselage of a small civil aircraft, an important load case is the so-called dynamic landing where, following the impact of the landing gear, the fuselage bends downwards due to the inertia forces, and the panel is compressed. In the *DAEDALOS* project, acceleration time histories were provided for a full aircraft FE model. The time history near the assumed panel location had frequencies between 10 and 15 Hz, which corresponds well to the lowest vibration mode that involves fuselage bending.

To simulate the operating conditions in the context of a fuselage structure, the panel is assumed clamped at one end and loaded at the opposite end with an imposed displacement. While the presence of the surrounding structure would suggest to impose symmetry conditions along the longitudinal edges, free edge conditions are here introduced. This choice, although less realistic, allows the comparison with FE results from other *DAEDALOS* project partners. However, quasi-static analysis showed that the load and stress levels are similar for symmetric and free sides, although the post-buckling pattern is different.

The loading function is:

$$\Delta U = -\frac{1.8\text{ mm}}{2}\left(1-\cos\left(\frac{\pi t}{0.025}\right)\right) \tag{22}$$

for $t < 0.05$ s and 0 thereafter (the simulation is run until 0.1 s). The function reaches its peak value of -1.8 mm, corresponding to an edge shortening of $3000 \cdot 10^{-6}$ micro-strain at 0.025 s. This smooth pulse approximates the first peak of the above-mentioned acceleration time history but is larger in amplitude.

4.5. *GMM parameter fitting for post-buckling simulations*

In the post-buckling field, the panel undergoes rapid movements, requiring a different set of GMM parameters than those described in section 3. Figure 6 shows the power spectrum of the stress evolution at a point in the panel (see also Figure 14).

The lowest free-vibration frequency of the panel is 242 Hz. With the chosen discretization, the highest free-vibration frequency is $\approx 5 \cdot 10^6$ Hz. For finer discretizations, the maximum frequency might be even higher, because the theory of continuum mechanics permits vibrations of infinite frequency. With an increment size of 10^{-5} s, the solver tracks vibrations up to ≈10 kHz. Vibrations beyond 5000 Hz have relatively short wavelengths, and their influence on the post-buckling behavior and on the amplitudes of the stress fluctuations can be neglected. To keep the computational effort at a practical level, it makes sense not to track high-frequency vibrations in great detail, but rather to dampen them with the GMM.

Because the maximum frequency for the DMA measurements is 50 Hz, the 3-parameter GMM described in section 3 is not sufficient. In absence of high-frequency experimental data,

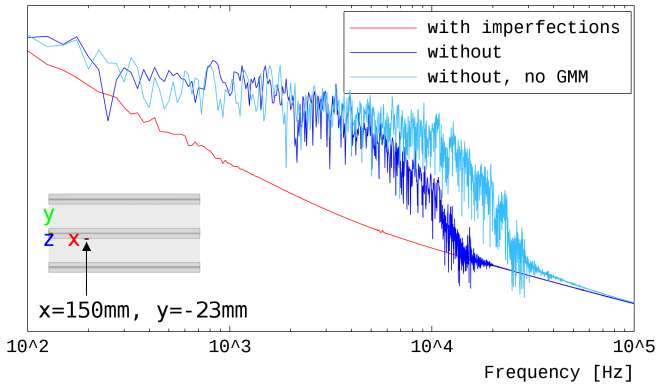

Figure 6: Logarithmic plot of the spectral power of the compressive stress in fiber direction, sampled with a very small time increment of 10^{-6} s, between 0.005 s and 0.045 s at a selected point in the skin. Red curve: Imperfect variant, GMM. Dark blue curve: Perfect variant, GMM. Light blue curve: Perfect variant, without GMM. The GMM parameters were obtained as is described in this section.

the loss modulus was kept constant above 50 Hz up to the frequency which corresponds to the smallest expected time increment. An additional data point was added at 10^8 Hz. It is useful however, to select a smaller minimum relaxation time, as this will result in a improved fitting. Spacing the relaxation times evenly, starting from $\tau_{0,j} = 10^{-9}$ s and doubling this value each time ($\tau_{i+1,j} = 2\tau_{i,j}$), 28 GMM parameters were needed.

Apart from a slightly higher computational effort, this large number of parameters did not pose any problems neither for the fitting procedure nor for the dynamic nonlinear solver. Figure 7 shows the results for the fiber direction.

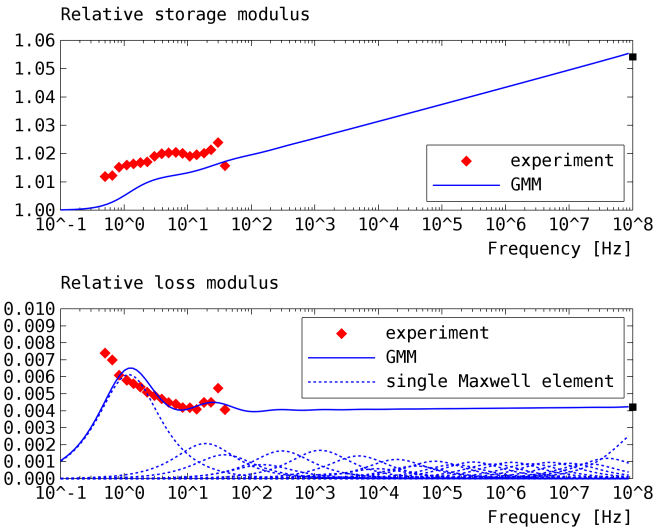

Figure 7: Hexcel® IM7/8552 relative storage and loss moduli in fiber direction ($j = 1$) and approximated GMM with 28 elements. Rhombic Dots: Measured. Rectangular dot: Additional. Solid lines: GMM. Dotted lines: Individual Maxwell elements.

4.6. Dynamic nonlinear solution procedure

The dynamic equilibrium equations contain, in addition to the external forces and the internal elastic forces, the viscous forces provided via the GMM, and the inertia forces. The two latter force terms provide the necessary stabilization to the tangent stiffness matrix. The nonlinear direct transient solver makes use of the backward differentiation formula (BDF) method, which is well suited to solve stiff ordinary differential equations (Shampine and Gear, 1979) like the ones encountered in shell structures. To achieve unconditional stability in the nonlinear regime, the second-order BDF is selected. For computational efficiency, the time increment size is adapted during the analysis using the transformation method of Nordsieck (1962). The increment size is controlled using Milne's device error estimator (Milne, 1970) in function of a user-defined dynamic tolerance, and the rate of increment of the increment size is limited (Calvo et al., 1987).

The automatic time increment size control means that the solver is suited to highly nonlinear problems. In the presence of rapid changes, the solver reduces the time increment accordingly. Conversely, when there are only small changes, the solver will increase the time increment. Thus, for problems with many vibrations or changes, the average time increment will be small and the computational effort will be large. On the other hand, nearly-static problems will require fewer time increments and will be quicker to solve.

The average time increment is controlled via the user-defined dynamic tolerance. A large dynamic tolerance value will result in a relatively fast simulation involving fewer time increments, while a small dynamic tolerance will need more time increments but will allow for higher accuracy.

This trade-off between computational effort and accuracy can be controlled by observing the time-integration error $\mathcal{E}(t)$ at time t which can be calculated from the difference

$$\mathcal{E}(t) = W(t) - T(t) - U(t) - D(t) \tag{23}$$

between the external work W, the total kinetic energy T, the total elastic energy U, and the total material dissipation D.

Only for a perfect solver (using infinitesimal time increments) will $\mathcal{E}(t)$ be zero. To allow for a reliable interpretation of the results, the dynamic tolerance should be chosen such that $\mathcal{E}(t) \ll D(t)$, see Figure 8.

Due to the small values of loss factors typical of CFRP structures, the time increments can be relatively small. The average time increment is $1.45 \cdot 10^{-5}$ s for the perfect panel and $9.5 \cdot 10^{-5}$ s for the panel with imperfections. For the loading conditions that were used, at least the time span between 0 s and 0.05 s should be calculated in dynamic analyses, as the peak stresses may occur after the full load is applied at 0.025 s. When compared to the quasi-static analyses, the total computational effort is increased by a factor of 10 and 3.5, respectively.

4.7. Kinetic energy and dissipation

In quasi-static analysis, the drop of load at first buckling for the perfect panel corresponds to $\approx$ 0.5 J loss in elastic energy. This is well reflected by the predicted kinetic energy in dynamic analysis which peaks at $\approx$ 0.25 J. Figures 9 and 10 show that the panel without imperfections develops a much more dynamic behavior in the post-buckling range than the panel with imperfections. When imperfections are present, no significant drop of load occurs, and the kinetic energy is much lower. There is also a difference in the vibration frequencies as the panel with geometric imperfections vibrates with a primary frequency of $\approx$ 700 Hz while those of the perfect panel is $\approx$ 2000 Hz. An exponential decay of the kinetic energy, $T_2/T_1 = \mathrm{e}^{-a\Delta t}$, can be observed between $T_1 = 0.05$ s and $T_2 = 0.1$ s, with $a \approx 25$ and $a \approx 45$ for the panel with and without geometric imperfections, respectively.

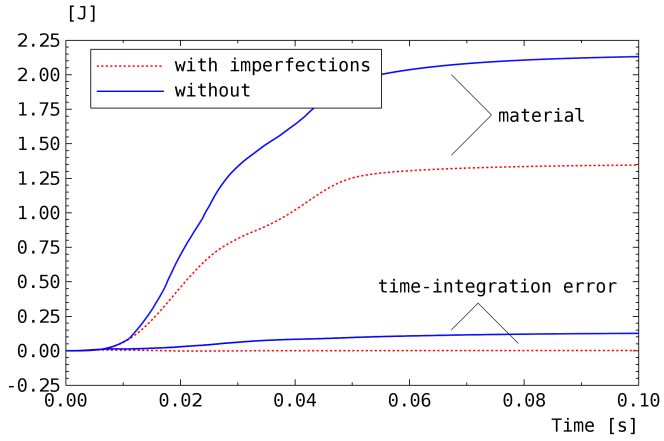

Figure 8: Material dissipation and approximate time-integration error with and without imperfections.

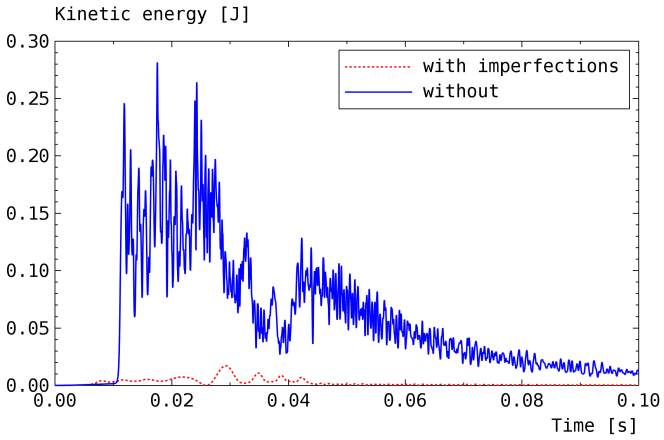

Figure 9: Evolution of the kinetic energy with and without geometric imperfections.

Figure 11 and Table 5 show how the material dissipation is distributed within the panel. It is non-uniform and follows the buckling pattern. The locally highest dissipation occurs in the flanges of the central stringer. For the panel without imperfections, there is a two-fold increase in the overall dissipation of the skin, while the overall dissipation of the stringers is similar. The difference between the amount of energy dissipated by the skin is due to the different deformed shapes observed for the

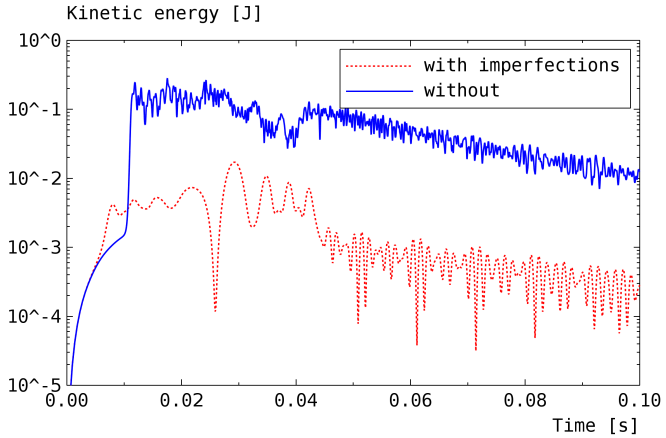

Figure 10: Logarithmic plot of the kinetic energy with and without geometric imperfections.

perfect and the imperfect panel during the time frame considered.

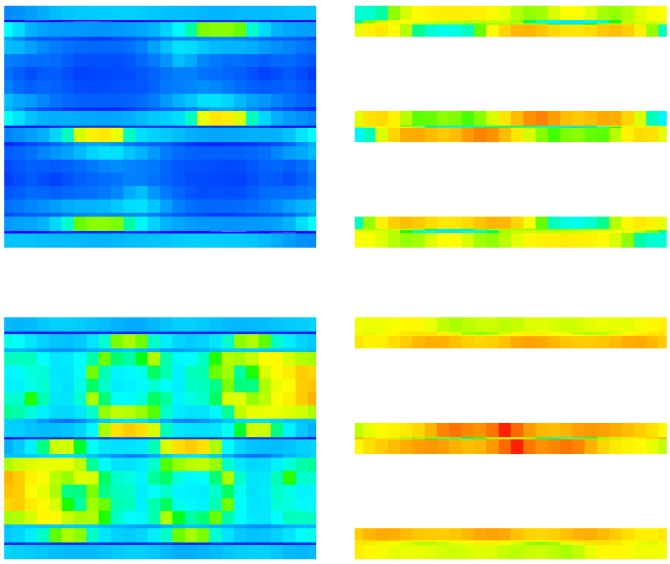

Figure 11: Material dissipation integrated over the time span between 0 s and 0.05 s, calculated separately for each finite element. Only the central part of 400 mm length is shown. Top left: Panel with imperfections, skin. Top right: Panel with imperfections, stringer. Bottom left: Perfect panel, skin. Bottom right: Perfect panel, stringer.

4.8. Evolution of stress

Despite the kinetic energies being small when compared to the elastic energies, they can cause large stress fluctuations. Figure 12 shows the evolution of the compressive stress of the whole panel for each time increment. The difference between the models with and without geometric imperfections is about 15%. No previous studies were found by the authors with regard to the comparison between the stress levels with and without imperfections. In general, the discrepancy between these two results is significant and illustrates that, in the context of a

	Skin	Flanges	Web	Total
With imperfections	0.406	0.445	0.401	1.252
Without	0.944	0.523	0.476	1.926

Table 5: Per-member total material dissipation in [J].

design phase, the final weight of the panel can be affected by the fact of accounting for initial imperfections. When experimental measures of the panel imperfections are unavailable, one possibility would be to assume the results of the perfect and imperfect configurations as the upper and lower bounds, respectively.

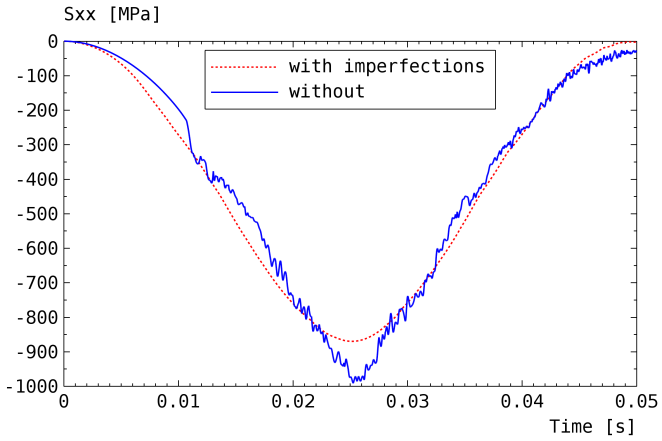

Figure 12: Evolution of highest (in absolute terms) compressive stress in fiber direction.

The differences are larger when looking at a single point. Figure 13 shows the stress near the center of the skin field. The sizes of the skin buckles are not identical, which explains the large difference in stress at this location. There is much fluctuation in the moderately high compressive stress of the perfect variant. The difference in the peak compression stress of the perfect and imperfect panels is noteworthy and highlights the importance of a proper imperfection modeling during the analysis phase. Indeed, the onset of an intralaminar damage mechanisms as well as the propagation of an already existent pre-damage are affected by the predicted stress level.

A more extreme situation is found in Figure 14, where the perfect panel exhibits three times higher compressive stresses than the panel with imperfections.

In general, the stress levels predicted for the panel with imperfections closely match those for a quasi-static analysis with stabilization and the same loading, as Figure 15 shows.

5. Conclusions

The present work has regarded the development of a methodology to account for damping effects in the nonlinear analysis of composite structures. The material characterization is based on DMA measurements, while a linear Generalized Maxwell Model (GMM) suited for transverse-isotropic CFRP, has been

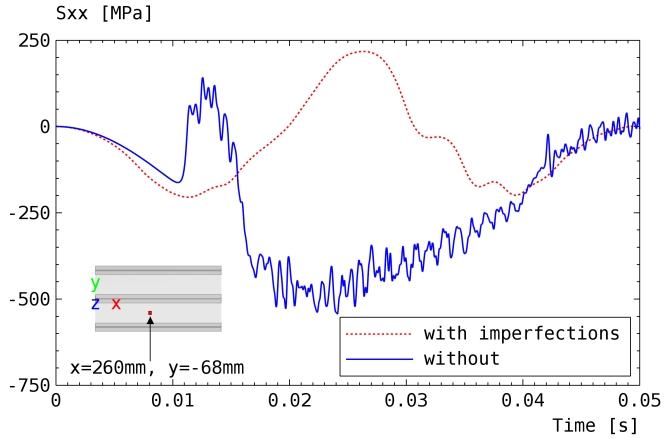

Figure 13: Evolution of the stress in fiber direction near the center of the skin field.

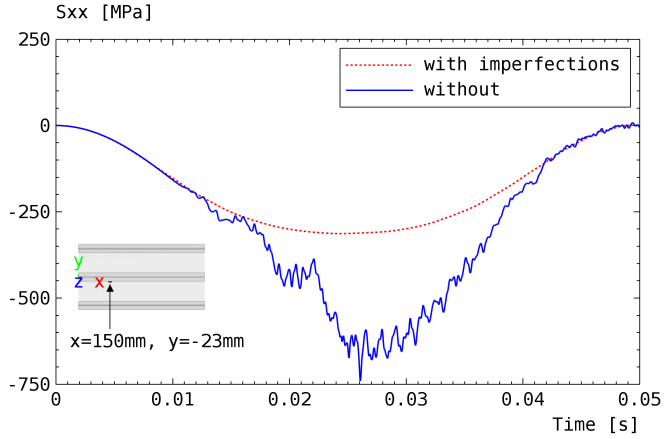

Figure 14: Evolution of the stress in fiber direction close to the stringer flange.

formulated and implemented within the B2000++ finite element package. Experimental DMA measurements of the storage and loss moduli were conducted, and the GMM parameters were fitted against these measurements, using a nonlinear optimization algorithm.

As compared to common analysis tools where damping is usually introduced at global level, the present implementation offers the advantage of allowing the description of local, nonlinear viscous effects that can influence the response of aeronautical panels operating in the post-buckling regime.

Within the proposed framework, another advantage is given by the possibility of characterizing the material viscoelastic behavior by means of simple material coupons. To illustrate a potential application of the method developed, an example was discussed regarding a curved composite panel stiffened by three stringers. Dynamic loading conditions consisting in a smooth compressive pulse load were assumed, and the simulations were performed considering two configurations, with and without imperfections, respectively.

The results allowed to illustrate the different steps of the procedure, providing a clear insight into the potentialities offered by the method. In particular, the effects of damping can be an-

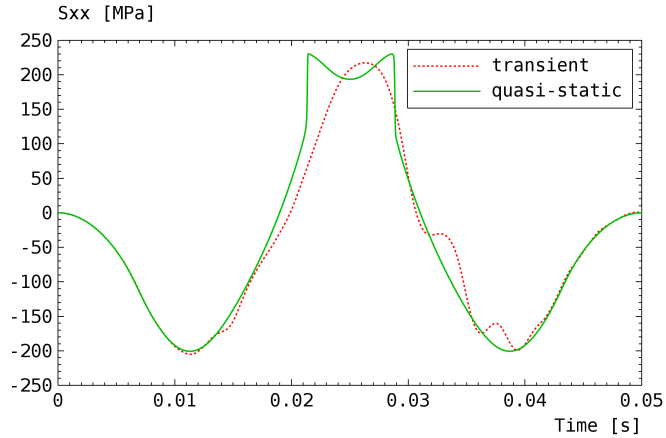

Figure 15: Comparison between transient and quasi-static non-linear analyses. Panel with imperfections and values at the same location as shown in Figure 13.

alyzed at a global level, in terms of force-displacement curves, and at local level. With this regard, local quantities such as the stress distribution as well as the contour of the dissipated energy in the different portion of structure could be analyzed. From the comparison between perfect and imperfect structure, the perfect panel represents, in this case, the worst-case scenario in terms of stress levels and the computational effort. On the other hand, the inertia effects in the panel with geometric imperfections are small, which makes it suitable to purely quasi-static analysis.

Acknowledgments

The research leading to these results has partially received funding from the European Union's Seventh Framework Programme [FP7/2007-2013] under grant agreement "DAEDALOS - Dynamics in Aircraft Engineering Design and Analysis for Light Optimized Structures" No. 266411.

References

Bisagni, C., Catapano, E., 8–11 April 2013. Strain energy method to model composite structures damping. In: 54^{th} AIAA/ASME/ASCE/AHS/ASC Structures, Structural Dynamics, and Materials Conference. AIAA-2013-1760. Boston, MA.

Bisagni, C., Vescovini, R., Dávila, C., 2011. Single-stringer compression specimen for the assessment of damage tolerance of postbuckled structures. Journal of Aircraft 48 (2), 495–502.

Bobillot, A., Balmes, E., 22–25 April 2002. Iterative techniques for eigenvalue solutions of damped structures coupled with fluids. In: 43^{rd} AIAA/ASME/ASCE/AHS/ASC Structures, Structural Dynamics, and Materials Conference. AIAA-2002-1391. Denver, CO.

Calvo, M., Lisbona, F., Montijano, J., 1987. On the stability of variable-stepsize nordsieck bdf methods. SIAM Journal on Numerical Analysis 24 (4), 844–854.

Camanho, P., Maimí, P., Dávila, C., 2007. Prediction of size effects in notched laminates using continuum damage mechanics. Composites Science and Technology 67 (13), 2715–2727.

Chandra, R., Singh, S., Gupta, K., 1999. Damping studies in fiber-reinforced composites–a review. Composite Structures 46 (1), 41–51.

Del Piero, G., Deseri, L., 1996. On the analytic expression of the free energy in linear viscoelasticity. Journal of Elasticity 43 (3), 247–278.

Enelund, M., Lesieutre, G., 1999. Time domain modeling of damping using anelastic displacement fields and fractional calculus. International Journal of Solids and Structures 36 (29), 4447–4472.

Gradowczyk, M., Moavenzadeh, F., 1969. Characterization of linear viscoelastic materials. Transactions of The Society of Rheology 13 (2), 173–191.

Johnson, S., 2010. The nlopt nonlinear-optimization package. `http://ab-initio.mit.edu/nlopt`.

McTavish, D., Hughes, P., 1993. Modeling of linear viscoelastic space structures. Journal of Vibration and Acoustics 115 (1), 103–110.

Melo, J., Radford, D., 2003. Viscoelastic characterization of transversely isotropic composite laminae. Journal of Composite Materials 37 (2), 129–145.

Melo, J., Radford, D., 2004. Time and temperature dependence of the viscoelastic properties of PEEK/IM7. Journal of Composite Materials 38 (20), 1815–1830.

Merazzi, S., Stehlin, P., 1977. Viscoelastic buckling of shells. In: Proceedings of the Colloquium on Numerical Analysis ISNM37. Vol. ISNM 37. Birkhäuser Verlag, Basel und Stuttgart, pp. 167–191.

Milne, W., 1970. Numerical Solution of Differential Equations. Dover Publications Inc, New York.

Nordsieck, A., 1962. On numerical integration of ordinary differential equations. Mathematics of Computation 16 (77), 22–49.

Schapery, R., 1961. A simple collocation method for fitting viscoelastic models to experimental data. GALCIT SM 61-23A,, California Institute of Technology.

Shampine, L., Gear, C., 1979. A user's view of solving stiff ordinary differential equations. SIAM review 21 (1), 1–17.

Simo, J., Hughes, T., 2000. Computational Inelasticity. Interdisciplinary Applied Mathematics. Springer, New York.

SMR S.A., 1999-2014. B2000++ User Manual.

Staverman, A., Schwarzl, F., 1952. Thermodynamics of viscoelastic behavior. Proceeding Academic Science of the Koninklijke Nederlandse Akademie van Wetenschappen Physical Sciences 55, 474–492.

Vasques, C., Moreira, R., Rodrigues, J., 2010. Viscoelastic damping technologies–part I: Modeling and finite element implementation. Mechanical Engineering 1 (2), 96–110.